

# Tracking ultrafast change of multiterahertz broadband response functions in a photoexcited Dirac semimetal Cd<sub>3</sub>As<sub>2</sub>

Natsuki Kanda<sup>1,2\*</sup>, Yuta Murotani<sup>1</sup>, Takuya Matsuda<sup>1</sup>, Manik Goyal<sup>3</sup>,  
Jun Yoshinobu<sup>1</sup>, Susanne Stemmer<sup>3</sup>, and Ryusuke Matsunaga<sup>1,2\*</sup>

<sup>1</sup>*The Institute for Solid State Physics, The University of Tokyo, Kashiwa, Chiba 277-8581, Japan.*

<sup>2</sup>*PRESTO, Japan Science and Technology Agency, 4-1-8 Honcho Kawaguchi, Saitama 332-0012, Japan.*

<sup>3</sup>*Materials Department, University of California, Santa Barbara, California 93106-5050, USA.*

\*e-mail: n-kanda@issp.u-tokyo.ac.jp, matsunaga@issp.u-tokyo.ac.jp

## Abstract

The electromagnetic response of Dirac semimetals in the infrared and terahertz frequency ranges is attracting growing interest for potential applications in optoelectronics and nonlinear optics. The interplay between the free-carrier response and interband transitions in the gapless, linear dispersion relation plays a key role in enabling novel functionalities. Here we investigate ultrafast dynamics in thin films of a photoexcited Dirac semimetal Cd<sub>3</sub>As<sub>2</sub> by probing the broadband response functions as complex quantities in the multiterahertz region (10-45 THz, 40-180 meV, or 7-30  $\mu$ m), which covers the crossover between the inter and intraband response. We resolve dynamics of the photoexcited nonthermal electrons which merge with originally existing carriers to form a single thermalized electron gas and how it is facilitated by high-density excitation. We also demonstrate that a large reduction of the refractive index by 80% dominates the nonequilibrium infrared response, which can be utilized for designing ultrafast switches in active optoelectronics.

## Introduction

Recently enormous research efforts have been devoted to investigating the novel properties of three-dimensional (3D) topological Dirac and Weyl semimetals that arise from topologically or symmetry protected relativistic electrons<sup>1,2</sup>. Nonlinear interaction with light is also highly intriguing because of its applicability to controlling the topological phase of matter by strong laser pulses<sup>3-5</sup>. In addition, their responses to light at room temperature are also drawing considerable attention for potential applications in nonlinear optics and optoelectronic devices, especially in mid-infrared (MIR), far-infrared, or terahertz (THz) frequency range because of their gapless band structure. Photocurrent generation from the near-infrared (NIR) to 10  $\mu\text{m}$  is expected to realize high-speed broadband photodetectors<sup>6-8</sup>. Saturation of absorption for intense NIR and MIR light has been incorporated in mode-locked pulsed lasers as ultrafast modulators<sup>9,10</sup>. Highly nonlinear current from accelerated massless electrons realizes efficient frequency conversion in THz regime<sup>11-13</sup>. Tunable, perfect absorbers with semimetal-based metamaterials were also proposed for THz sensing and filters<sup>14,15</sup>. Low-frequency stimulated emission is also expected for use in an infrared gain medium in a similar way to graphene<sup>16,17</sup>. Compared to graphene, which consists of a single atomic monolayer, the large interaction volume with light, the feasibility of fabricating large-area thin films, and the robustness to the environment make 3D topological semimetals advantageous for these applications.

To thoroughly explore these novel functionalities, an in-depth understanding of the responses away from equilibrium is indispensable. Significant attention has focused on the ultrafast carrier dynamics of  $\text{Cd}_3\text{As}_2$ , a prototypical 3D Dirac semimetal with a large carrier mobility, high Fermi velocity, chemical stability, low Fermi level, and quasi-linear band character in a wide energy scale<sup>18</sup>. Pump-probe spectroscopy studies in  $\text{Cd}_3\text{As}_2$  have been reported in the NIR<sup>19</sup>, MIR<sup>9,20-23</sup> and at THz frequencies<sup>11,24-26</sup>, but there are some controversies. For example, the relaxation dynamics is analyzed typically within the two-temperature model (TTM), which provides the time evolution of temperatures in the electron and lattice subsystems. Whether one can define the electron temperature, *i.e.*, the time scale of establishing a hot Fermi-Dirac distribution from photoexcited nonthermal electrons, is an issue to be resolved. Some studies assumed that it should be much faster than 100 fs as in usual metals<sup>20,22</sup>. In other studies<sup>19,21</sup>, however, a decay component at several hundred fs was attributed to the scattering time to establish a hot carrier distribution. Prior time-resolved MIR experiments have been performed by probing the intensity of transmitted or reflected pulses and therefore require careful treatments to derive the complex response function in the frequency space. Information on the complex response functions is particularly important in semimetals, because in addition to absorption, the permittivity described by the real-part dielectric function,  $\epsilon_1(\omega)$ , is also essential in their infrared response. Figures 1a and 1b show the optical absorption spectrum  $\sigma_1(\omega)$  (semi-log plot) and the real-part dielectric function  $\epsilon_1(\omega)$  in  $\text{Cd}_3\text{As}_2$ , respectively

(details are described below). Across the screened plasma frequency, located at 10 THz, metallic screening ( $\epsilon_1 < 0$ ) changes to dielectric screening ( $\epsilon_1 > 0$ ) with flipping its sign. When carriers are photoinjected into the semimetal, the plasma frequency is elevated, accompanied with large modulation of  $\epsilon_1$  and refractive index  $n$ , which drastically alters the boundary condition of light for infrared interband transition. THz time-domain spectroscopy can directly probe the response function without Kramers-Kronig conversion, but only for the DC-limit response with limited time resolution of  $\sim 1$  ps. Therefore, for a comprehensive understanding of the interplay between inter and intraband transitions, it is important to track ultrafast change of nonequilibrium response functions as complex quantities within a broad energy scale from several tens to a few hundreds of meV, i.e., multiterahertz frequency range from 10 to several tens of THz<sup>27,28</sup>.

In this work, we investigated the ultrafast dynamics of a photoexcited Cd<sub>3</sub>As<sub>2</sub> thin film by probing transmittance in the multiterahertz range (10-45 THz in frequency, 40-180 meV in energy, or 7-30  $\mu\text{m}$  in wavelength). Broadband time-domain spectroscopy allows us to directly evaluate ultrafast changes of the response functions at the crossover region of inter and intraband transitions. After NIR photoexcitation, we resolve transient spectra of induced absorption and loss function, which are significantly deformed at the initial stage, clarifying the thermalization timescale of photoexcited electrons. We also elucidate a large suppression of the refractive index, which plays a dominant role in the infrared response of the photoexcited Dirac semimetal.

## Results

**Sample.** The sample is an epitaxially-grown, (112)-oriented Cd<sub>3</sub>As<sub>2</sub> thin film with 140-nm thickness on an 800- $\mu\text{m}$ -thick CdTe substrate<sup>29-31</sup>. Figure 1c shows the model calculation of the band structure of Cd<sub>3</sub>As<sub>2</sub>, which has two Dirac nodes near the  $\Gamma$  point along the [001] directions<sup>32</sup>. Note that the linear dispersion relation of electrons associated with the symmetry-protected Dirac nodes in Cd<sub>3</sub>As<sub>2</sub> is limited to a small energy scale of meV, and that the dispersion relation in the multiterahertz scale at a few hundreds of meV is described by the massless-like Kane model<sup>33</sup>. The linear response function of the film was evaluated by THz time-domain spectroscopy and Fourier-transform infrared spectroscopy (see Methods section). All experiments in this work were performed at room temperature. The thick solid curves in Figs. 1a and 1b show the experimental results of the conductivity spectrum  $\sigma_1(\omega)$  and dielectric function  $\epsilon_1(\omega)$ , respectively. The red curve shows an interpolated fit by assuming the Drude-type response (green) and the interband transition linear to frequency with the step-like onset at  $2E_F$  (blue), which gives a Fermi energy of  $E_F = 58$  meV (see Supplementary Text S2). We also checked the polarization dependence and concluded that in-plane anisotropy is

negligibly small in our frequency window at room temperature owing to the quasi-3-fold rotational symmetry of the (112) surface.

**Pump-probe spectroscopy.** To explore ultrafast dynamics after photoexcitation, we conducted pump-probe spectroscopy. Figure 1d shows a schematic of the experimental setup (see Methods section). The light source is a Yb:KGW-based regenerative amplifier with a centre frequency of 1030 nm, a repetition rate of 3 kHz, a pulse energy of 2 mJ, and a pulse width of 255 fs. A portion of the output was compressed to <14 fs by using the multi-plate broadening scheme<sup>34,35</sup> and was further split to generate multiterahertz pulses and gate pulses. Figures 1e and 1f show the waveform and the power spectrum of multiterahertz pulses, which covers the broad bandwidth of 10-45 THz with the pulse duration of 28 fs. After transmission through the sample, the multiterahertz pulses were detected by electro-optic sampling. A residual laser output was sent to an optical parametric amplifier system to generate pump pulses with 2- $\mu$ m wavelength (0.62 eV, 150 THz) and 230-fs pulse duration.

**Dynamics of thermalization.** Figure 2a shows the two-dimensional (2D) plot of differential transmittance  $\Delta T/T$  as functions of frequency (horizontal) and pump delay (vertical). The pump fluence is 25  $\mu\text{J}/\text{cm}^2$ , which we refer to a weak excitation condition. If one assumes that a Fermi-Dirac electron distribution is developed after photoexcitation with an elevated electron temperature, the TTM analysis gives a maximum electron temperature of 330 K for this pump fluence (see Supplementary Text S1). The red- and blue-colored data show that  $\Delta T$  tends to be positive at higher frequencies and negative at lower frequencies, respectively. Figure 2b shows the 2D plot of differential absorption spectra, *i.e.*, the change of the real-part conductivity  $\Delta\sigma_1$ . The red and blue colors correspond to bleaching ( $\Delta\sigma_1 < 0$ ) and induced absorption ( $\Delta\sigma_1 > 0$ ), respectively. Sequential spectral profiles of  $\Delta\sigma_1$  at several pump delays are also plotted in Fig. 2c. The green color indicates the timing of pump pulse irradiation. Right after the pump, induced absorption appears, which can be ascribed to absorption by photoexcited carriers. Notably, the induced absorption spectrum at 0.2 ps spreads over a wide frequency range, which cannot be attributed to be solely due to heating of electrons to the elevated temperature of 330 K. Subsequently, the spectral weight concentrates into the lower-frequency side to form a Drude-type spectrum, which occurs at the time scale of 0.5 ps. Simultaneously, the bleaching is also discerned at the higher frequency above 25 THz ( $\sim 100$  meV), which can be ascribed to the Pauli blocking in the interband transition. After that, the overall signal starts to decay while keeping its spectral shape.

We also plot the time evolution of  $-\text{Im}(\epsilon^{-1})$  in Fig. 2d. This is the loss function in the small wavevector limit and gives a peak of the longitudinal plasmon mode at the screened plasma frequency<sup>36</sup>, which is located at 10 THz in equilibrium. Right after the photoexcitation, the loss

function is significantly deformed and spread into higher frequency while leaving a spectral weight in the low frequency. The deformed spectrum indicates that the response is not well described by a simple Drude model, suggesting that photoexcited electrons in the initial stage are quite nonthermal and behave differently from originally existing electrons. After undergoing repeated scattering, they should be thermalized to form a single hot electron gas with a well-defined electron temperature. Indeed, the experimental result in Fig. 2d after  $\sim 0.5$  ps shows that a single peak develops at 20 THz, indicating that a single collective plasmon mode becomes well defined at this time scale with an elevated plasma frequency. The result clarifies that the thermalization timescale of photoexcited electrons is as long as 0.5 ps. It is consistent with previous pump-probe studies<sup>19,21</sup> where a decay component of  $\sim 0.5$  ps observed only in degenerate pump and probe energies was attributed to the thermalization process.

Figures 2e-2h show the data with a stronger excitation density of  $250 \mu\text{J}/\text{cm}^2$ , which corresponds to the maximum electron temperature of 730 K (see Supplementary Text S1). Compared to the results in the weak excitation regime in Fig. 2d, the loss function peak in Fig. 2h develops at 35 THz because of increased carrier density. In addition, the peak is significantly broadened, indicating that the scattering rate between the high-density carriers is enhanced. Correspondingly, the time scale of developing the single loss function peak is as short as 0.3 ps after the photoexcitation, which is faster than that in the weak excitation regime. It can be reasonably explained by the enhanced scattering between a high density of carriers, which facilitates thermalization in the electron system.

**Dynamics after thermalization.** Next, we focus on the dynamics after thermalization. Figures 3a and 3b show the results of the real- and imaginary-part conductivity spectra  $\sigma_1$  and  $\sigma_2$  with the pump fluence of  $50 \mu\text{J}/\text{cm}^2$  at various delays. The data are fitted well by thin curves assuming the Drude-type response and the reduced interband transition, which gives the dynamics of total carrier density as plotted in Fig. 3c. In the weak excitation regime, the decay is well fitted by a single-exponential function. For higher excitation density  $>100 \mu\text{J}/\text{cm}^2$ , a double-exponential function is required to fit a fast decay component (see Supplementary Text S4). Figure 3d shows the decay constants as a function of the pump fluence. The slower decay constant  $\tau_{\text{slow}}$  is around 10 ps in the weak-excitation limit and shortened to be  $\sim 8$  ps in the high-density excitation. The results are consistent with or a bit longer than previous reports<sup>9,11,19-26</sup> and can be attributed to the carrier relaxation time interacting with the lattice system described by TTM (see Supplementary Text S1). The fast decay component  $\tau_{\text{fast}}$ , observed only in the high-density excitation regime, is as fast as few hundred fs and not fully resolved due to the time resolution of the pump pulse. The fast decay may be attributed to Auger recombination, *i.e.*, electron-electron scattering decreases the carrier density. Figure 3e shows the total carrier density as a function of the pump fluence, and the weights of the fast-

and slow-decay components were separately indicated. The result shows that the fast decay appears only when the total carrier density reaches to  $\sim 10^{19} \text{ cm}^{-3}$ , which corresponds to  $\sim 10^{14} \text{ cm}^{-2}$  in terms of the sheet carrier density of the thin film. It is in a stark contrast to graphene, where the Auger recombination dominates the carrier relaxation due to efficient collinear scattering<sup>37,38</sup> even for much smaller sheet carrier density<sup>39,40</sup>. A recent theory shows that the Auger scattering is prohibited in 3D linear dispersions because of nondivergent matrix element in contrast to the 2D counterpart<sup>41</sup>. The electron dispersion relation in  $\text{Cd}_3\text{As}_2$  in the multiterahertz energy scale is described by the Kane model with a nonvanishing parabolicity, which would allow to some degree of Auger scattering for high-density excitation.

Here we focus on the Pauli blocking signal ( $\Delta\sigma_1 < 0$ ), *i.e.*, photoexcited electrons occupying the conduction band that prohibit further interband transitions. One could expect that, under strong pump,  $\Delta\sigma_1 < 0$  could be so significant that  $\sigma_1$  might flip its sign to negative at the onset of the interband transition, which is the stimulated emission by inverted population<sup>16</sup>. We examined this point with various pump fluences but have not identified the  $\sigma_1 < 0$  signal in the present experimental conditions. The difficulty of the stimulated emission in the multiterahertz frequency range may be ascribed to (i) the tail of the Drude-type absorption broadened at the high-density excitation, and (ii) the limited phase space for the low-energy interband transition in the 3D quasi-linear dispersion. Stimulated emission may be realized at much higher frequency in NIR and MIR as reported in graphene by measuring transient NIR reflectance<sup>17</sup>. Among similar systems with massless-like Kane electrons, the multiterahertz stimulated emission has been achieved in a narrow-gap semiconductor  $\text{Hg}_{1-x}\text{Cd}_x\text{Te}$  with quantum well structure at cryogenic temperature<sup>42,43</sup>. For  $\text{Cd}_3\text{As}_2$ , reducing the film thickness can change the band structure to a gapped topological insulator<sup>44</sup>. Such a band structure engineering may enhance the possibility of realizing the light amplification because of increased density of states and suppressed recombination.

**Discussion.** Comparing Figs. 2a and 2b, the sign of  $\Delta T/T$  does not always coincide with the sign of  $\Delta\sigma_1$ , *i.e.*, the transmittance can increase even if the absorption also increases. This can be explained by decrease of reflection. Figures 4a-4d show the change in transmittance  $\Delta T/T$ , the real-part dielectric function  $\epsilon_1$ , the refractive index  $n$ , and the extinction coefficient  $\kappa$ , respectively, for various delays with the pump fluences of  $50 \mu\text{J}/\text{cm}^2$ . The black curves show the data before the pump, and it changes to the red, and relaxes to the green and blue curves in time. The photoinjection of carriers elevates the screened plasma frequency at  $\epsilon_1=0$  from 10 THz to a few tens of THz as shown in Fig. 4b. Accordingly,  $\epsilon_1$  and the refractive index  $n$  in the multiterahertz regime significantly decreases, which suppresses the reflection loss at the surface.

Our results demonstrating the large decrease of  $n$  is in line with the interpretation of the recent ultrafast reflectivity measurement<sup>22</sup> probed at 2.8-4.4  $\mu\text{m}$  (70-110 THz). Note that the analysis in Ref. 22 assumes that the extinction coefficient  $\kappa$  is proportional to the absorption. Strictly speaking, however,  $\kappa$  is defined as the spatial decay rate of the field due to both absorption and reflection and therefore is equal to  $\text{sgn}(\epsilon_2)\sqrt{\sqrt{\epsilon_1^2 + \epsilon_2^2} - \epsilon_1}/\sqrt{2}$ . Since the permittivity  $\epsilon_1 \sim 17$  and the absorption  $\epsilon_2 \sim 4$  are comparable at MIR in  $\text{Cd}_3\text{As}_2$ <sup>31</sup> and they can be significantly modified by photoexcitation, the assumption in Ref. 24 may not be necessarily justified. Our time-domain spectroscopy directly provides spectral information of  $\epsilon_1$  and  $\epsilon_2$  ( $= \sigma_1/\epsilon_0\omega$ ), and thus quantitatively corroborates the reduction of  $n$ .

Figure 4e shows the 2D plot of  $n$  as a function of frequency and pump delay at the pump fluence of 50  $\mu\text{J}/\text{cm}^2$ . Figure 4f shows the dynamics of  $n$  at 20 THz, showing a drastic reduction from 4.7 to 0.80. Since  $n$  is larger than  $\kappa$  and the penetration depth in this frequency is as large as several  $\mu\text{m}$  in this multiterahertz frequency scale, the infrared response of thin films can be dominated by  $n$  rather than  $\kappa$ . Therefore, the transient broadband small refractive index may be utilized for designing ultrafast optical switches. Recovery time of the reduced refractive index is determined by the carrier lifetime, which is  $\sim 10$  ps in  $\text{Cd}_3\text{As}_2$  and can be further shortened to 1 ps by doping for high-speed response<sup>9</sup>. Note that such a large reduction of  $n$  itself around the plasma frequency can be expected in any photoexcited semiconductors. How much the refractive index is reduced and how broadly this occurs in frequency space depends on the scattering, because a short scattering rate elongates the tail of the Drude-type absorption and prevents  $n$  from anomalous decrease. Although the scattering rate is enhanced in photoexcited  $\text{Cd}_3\text{As}_2$  as it is in usual semiconductors, it tends to be robust against carrier density in topological materials with linear dispersion<sup>45</sup>. If one can use another topological semimetal with scattering time insensitive to the carrier density, it would realize unprecedented controllability of infrared response functions for novel optoelectronics and active metamaterials.

In summary, we conducted time-resolved spectroscopy for a photoexcited  $\text{Cd}_3\text{As}_2$  thin film in the multiterahertz frequency region. Ultrafast probe of the broadband response functions clarified the dynamics of photoexcited carriers with thermalization and relaxation processes in  $\text{Cd}_3\text{As}_2$ . We also quantitatively demonstrated a large suppression of the refractive index by more than 80% due to the reduced permittivity and sharp Drude response. The results provide valuable information for designing infrared high-speed optoelectronic devices as well as for control of topological phase of matter by infrared light.

## Methods

**Sample preparation.** A (112)-oriented Cd<sub>3</sub>As<sub>2</sub> film was grown by molecular beam epitaxy (MBE) on a (111)B CdTe substrate with a 3° miscut, as described in detail elsewhere<sup>46</sup>. The film thickness was about 140–150 nm, as determined from the growth time. At room temperature, the Hall mobility of the film was ~10,000 cm<sup>2</sup>/Vs.

### Evaluation of linear response function.

Linear response functions in the low-frequency regime (0.5–3 THz) were evaluated by conventional THz time-domain spectroscopy, which was based on a Yb:KGW-based regenerative amplifier laser system with (110) GaP crystals for THz pulse generation and detection. For the higher-frequency regime (15–50 THz), Fourier-transform infrared spectroscopy system (FT/IR-6600 and IRT-5200, JASCO) was used for transmission and reflection. Transmittance and reflectance can be expressed as functions of complex refractive indices by considering Fresnel coefficients, propagation loss, and multireflection. By employing the Newton-Raphson method, the complex refractive indices of a CdTe substrate and a Cd<sub>3</sub>As<sub>2</sub> film at each frequency were solved (see Supplementary Text S2 for more detail). We evaluated the scattering time of 120 fs, the plasma frequency of 51.2 THz, and the Fermi energy shift  $E_F$  of 58 meV, which are in good accordance with previous FTIR measurement of a similar film<sup>31</sup>. The carrier density was estimated as  $1 \times 10^{18}$  cm<sup>-3</sup>, assuming the effective mass of  $0.03m_e$ <sup>46,47</sup>.

### Pump-probe spectroscopy.

Light source is a Yb:KGW-based regenerative amplifier with the centre frequency of 1030 nm, the repetition rate of 3 kHz, the pulse energy of 2 mJ, and the pulse width of 255 fs. A portion of output (0.4 mJ) was compressed to <14 fs with a throughput of 70 μJ by using two-stage multi-plate broadening scheme with glass plates and chirped mirrors<sup>34,35</sup>. It was further split to generate multiterahertz pulses and gate pulses. Multiterahertz pulses were emitted from a 30-μm-thick GaSe crystal via intra-pulse differential frequency generation. After transmitting the sample, multiterahertz pulses were detected by the electro-optic sampling with gate pulses in a few-μm-thick GaSe flake which was deposited on a diamond substrate to suppress internal reflections<sup>48</sup>. A residual laser output was sent to an optical parametric amplifier system to generate pump pulses with 2-μm wavelength (0.62 eV, 150 THz) and 230-fs pulse duration. The probe pulse was focused on the sample with an off-axis parabolic mirror, while the pump pulse was delivered to the sample from the outside of the parabolic mirror with the non-colinear angle of 15°. Penetration depth of the pump in Cd<sub>3</sub>As<sub>2</sub> is 180 nm<sup>49</sup>, which is larger than the film thickness, and the spot sizes (full width of 1/e<sup>2</sup> maximum in intensity) of the pump and probe were 2.6 mm and 46 μm, respectively, so that inhomogeneous excitation was avoided. The pump photon energy also inhibits two-photon absorption in the substrate with the band



gap of 1.44 eV. By using a bare substrate, we confirmed that the effect of multi-photon absorption in the substrate is negligible at the excitation intensity used in this work. For the pump-probe spectroscopy, the optical path length of the gate pulses was fixed, and the time delay for the multiterahertz probe was scanned to obtain the field waveform for Fourier analysis of the response functions. The delay of the pump was scanned to investigate ultrafast dynamics after photoexcitation. It should be noted that the pump delay was corrected for each frequency in our analysis, considering the dispersion of the refractive index of a CdTe substrate (see Supplementary Text S3).

## Data availability

The data that support the findings of this study are available from the corresponding authors upon reasonable request.

## References

- [1] Armitage, N. P., Mele, E. J., and Vishwanath, A. Weyl and Dirac semimetals in three-dimensional solids, *Rev. Mod. Phys.* **90**, 015001 (2018).
- [2] Lv, B. Q., Qian, T., and Ding, H. Experimental perspective on three-dimensional topological semimetals, *Rev. Mod. Phys.* **93**, 025002 (2021).
- [3] Hübener, H., Sentef, M. A., De Giovannini, U., Kemper, A. F., and Rubio, A. Creating stable Floquet–Weyl semimetals by laser-driving of 3D Dirac materials, *Nat. Commun.* **8**, 13940 (2017).
- [4] Sie, E. J. et al. An ultrafast symmetry switch in a Weyl semimetal, *Nature* **565**, 61-66 (2019).
- [5] Vaswani, C. et al. Light-Driven Raman Coherence as a Nonthermal Route to Ultrafast Topology Switching in a Dirac Semimetal, *Phys. Rev. X* **10**, 021013 (2020).
- [6] Wang, Q. et al. Ultrafast Broadband Photodetectors Based on Three-Dimensional Dirac Semimetal Cd<sub>3</sub>As<sub>2</sub>, *Nano Lett.* **17**, 834-841 (2017).
- [7] Yang, M. et al. Enhanced Performance of Wideband Room Temperature Photodetector Based on Cd<sub>3</sub>As<sub>2</sub> Thin Film/Pentacene Heterojunction, *ACS Photon.* **5**, 3438-3445 (2018).
- [8] Liu, J., Xia, F., Xiao, D., Javier García de Abajo, F., and Sun, D. Semimetals for high-performance photodetection, *Nat. Mater.* **19**, 830-837 (2020).
- [9] Zhu, C. et al. A robust and tuneable mid-infrared optical switch enabled by bulk Dirac fermions, *Nat. Commun.* **8**, 14111 (2017).
- [10] Meng, Y. et al. Three-dimensional Dirac semimetal thin-film absorber for broadband pulse generation in the near-infrared, *Opt. Lett.* **43**, 1503-1506 (2018).

- [11] Cheng, B. et al. Efficient Terahertz Harmonic Generation with Coherent Acceleration of Electrons in the Dirac Semimetal  $\text{Cd}_3\text{As}_2$ , *Phys. Rev. Lett.* **124**, 117402 (2020).
- [12] Kovalev, S. et al. Non-perturbative terahertz high-harmonic generation in the three-dimensional Dirac semimetal  $\text{Cd}_3\text{As}_2$ , *Nat. Commun.* **11**, 2451 (2020).
- [13] Lim, J. et al. Efficient generation of extreme terahertz harmonics in three-dimensional Dirac semimetals, *Phys. Rev. Research* **2**, 043252 (2020).
- [14] Liu, G. D. et al. Dirac semimetals based tunable narrowband absorber at terahertz frequencies, *Opt. Express* **26**, 11471-11480 (2018).
- [15] Luo, J. et al. Ultrasensitive tunable terahertz sensor based on five-band perfect absorber with Dirac semimetal, *Opt. Express* **27**, 20165-20176 (2019).
- [16] Ryzhii, V., Ryzhii, M., and Otsuji, T. Negative dynamic conductivity of graphene with optical pumping, *J. Appl. Phys.* **101**, 083114 (2007).
- [17] Li, T. et al. Femtosecond Population Inversion and Stimulated Emission of Dense Dirac Fermions in Graphene, *Phys. Rev. Lett.* **108**, 167401 (2012).
- [18] Crassee, I., Sankar, R., Lee, W.-L., Akrap, A., and Orlita, M. 3D Dirac semimetal  $\text{Cd}_3\text{As}_2$ : A review of material properties, *Phys. Rev. Mater.* **2**, 120302 (2018).
- [19] Weber, C. P. et al. Transient reflectance of photoexcited  $\text{Cd}_3\text{As}_2$ , *Appl. Phys. Lett.* **106**, 231904 (2015).
- [20] Lu, W. et al. Ultrafast relaxation dynamics of photoexcited Dirac fermions in the three-dimensional Dirac semimetal  $\text{Cd}_3\text{As}_2$ , *Phys. Rev. B* **95**, 024303 (2017).
- [21] Zhu, C. et al. Broadband hot-carrier dynamics in three-dimensional Dirac semimetal  $\text{Cd}_3\text{As}_2$ , *Appl. Phys. Lett.* **111**, 091101 (2017).
- [22] Zhai, G. et al. Mid-infrared transient reflectance study of the Dirac semimetal  $\text{Cd}_3\text{As}_2$  under strong optical pumping, *Phys. Rev. B* **101**, 174310 (2020).
- [23] Zhai, G. et al. Photoexcited carrier dynamics of thin film  $\text{Cd}_3\text{As}_2$  grown on a GaAs(111)B substrate by molecular beam epitaxy, *Phys. Rev. B* **104**, 094302 (2021).
- [24] Lu, W., Ling, J., Xiu, F., and Sun, D. Terahertz probe of photoexcited carrier dynamics in the Dirac semimetal  $\text{Cd}_3\text{As}_2$ , *Phys. Rev. B* **98**, 104310 (2018).
- [25] Zhang, W. et al. Ultrafast photocarrier dynamics in a 3D Dirac semimetal  $\text{Cd}_3\text{As}_2$  film studied with terahertz spectroscopy, *Appl. Phys. Lett.* **114**, 221102 (2019).
- [26] Dai, Z. et al. High Mobility 3D Dirac Semimetal ( $\text{Cd}_3\text{As}_2$ ) for Ultrafast Photoactive Terahertz Photonics, *Adv. Func. Mater.* **31**, 2011011 (2021).
- [27] Junginger, F. et al. Single-cycle multiterahertz transients with peak fields above 10 MV/cm, *Opt. Lett.* **35**, 2645-2647 (2010).
- [28] Pashkin, A. et al. Ultrafast insulator-metal phase transition in  $\text{VO}_2$  studied by multiterahertz spectroscopy, *Phys. Rev. B* **83**, 195120 (2011).
- [29] Schumann, T., Goyal, M., Kim, H., and Stemmer, S. Molecular beam epitaxy of  $\text{Cd}_3\text{As}_2$  on a III-V substrate, *APL Mater.* **4**, 126110 (2016).

- [30] Schumann, T., Goyal, M., Kealhofer, D. A., and Stemmer, S. Negative magnetoresistance due to conductivity fluctuations in films of the topological semimetal  $\text{Cd}_3\text{As}_2$ , *Phys. Rev. B* **95**, 241113(R) (2017).
- [31] Chorsi, H. T. et al. Widely Tunable Optical and Thermal Properties of Dirac Semimetal  $\text{Cd}_3\text{As}_2$ , *Adv. Opt. Mater.* **8**, 1901192 (2020).
- [32] Wang, Z., Weng, H., Wu, Q., Dai, X., and Fang, Z. Three-dimensional Dirac semimetal and quantum transport in  $\text{Cd}_3\text{As}_2$ , *Phys. Rev. B* **88**, 125427 (2013).
- [33] Akrap, A. et al. Magneto-Optical Signature of Massless Kane Electrons in  $\text{Cd}_3\text{As}_2$ , *Phys. Rev. Lett.* **117**, 136401 (2016).
- [34] Lu, C.-H. et al. Generation of intense supercontinuum in condensed media, *Optica* **1**, 400-406 (2014).
- [35] Kanda, N., Ishii, N., Itatani, J., and Matsunaga, R. Optical parametric amplification of phase-stable terahertz-to-mid-infrared pulses studied in the time domain, *Opt. Express* **29**, 3479-3489 (2021).
- [36] Huber, R. et al. How many-particle interactions develop after ultrafast excitation of an electron-hole plasma, *Nature* **414**, 286-289 (2001).
- [37] Breusing, M. et al. Ultrafast nonequilibrium carrier dynamics in a single graphene layer. *Phys. Rev. B* **83**, 153410 (2011).
- [38] Brida, D. et al. Ultrafast collinear scattering and carrier multiplication in graphene. *Nat. Commun.* **4**, 1987 (2013).
- [39] Rana, F. Electron-hole generation and recombination rates for Coulomb scattering in graphene, *Phys. Rev. B* **76**, 155431 (2007).
- [40] Winzer, T., Knorr, A., and Malic, E. Carrier multiplication in graphene. *Nano Lett.* **10**, 4839-4843 (2010).
- [41] Afanasiev, A. N., Greshnov, A. A., and Svintsov, D. Relativistic suppression of Auger recombination in Weyl semimetals, *Phys. Rev. B* **99**, 115202 (2019).
- [42] Morozov, S. V. et al. Long wavelength stimulated emission up to  $9.5\ \mu\text{m}$  from HgCdTe quantum well heterostructures, *Appl. Phys. Lett.* **108**, 092104 (2016).
- [43] Morozov, S. V. et al. Stimulated emission from HgCdTe quantum well heterostructures at wavelengths up to  $19.5\ \mu\text{m}$ , *Appl. Phys. Lett.* **111**, 192101 (2017).
- [44] Schumann, T. et al. Observation of the quantum Hall effect in confined films of the three-dimensional Dirac semimetal  $\text{Cd}_3\text{As}_2$ , *Phys. Rev. Lett.* **120**, 016801 (2018).r
- [45] Yang, X. et al. Nanomaterial-Based Plasmon-Enhanced Infrared Spectroscopy, *Adv. Mater.* **30**, 1704896 (2018).
- [46] Goyal, M. et al. Thickness dependence of the quantum Hall effect in films of the three-dimensional Dirac semimetal  $\text{Cd}_3\text{As}_2$ , *APL Mater.* **6**, 026105 (2018).
- [47] Cheng, B. et al. A Large Effective Phonon Magnetic Moment in a Dirac Semimetal, *Nano Lett.* **20**, 5991–5996 (2020).

[48] Knorr, M. et al. Ultrabroadband etalon-free detection of infrared transients by van-der-Waals contacted sub-10- $\mu\text{m}$  GaSe detectors, *Opt. Express* **26**, 19059-19066 (2018).

[49] Neubauer, D. et al. Interband optical conductivity of the [001]-oriented Dirac semimetal  $\text{Cd}_3\text{As}_2$ , *Phys. Rev. B* **93**, 121202(R) (2016).

## **Acknowledgments**

This work was supported by JST PRESTO (Grant Nos. JPMJPR20LA and JPMJPR2006), JST CREST (Grant No. JPMJCR20R4), and in part by JSPS KAKENHI (Grants Nos. JP19H01817 and JP20J01422, and JP20H00343). R.M. also acknowledges partial support by Attosecond lasers for next frontiers in science and technology (ATTO) in Quantum Leap Flagship Program (MEXT Q-LEAP).

## **Author contributions**

R.M. conceived this project. M.G. and S.S. fabricated the sample. N.K. and T.M. evaluated the linear response function. N.K. developed the pump-probe spectroscopy system, performed the experiments, and analyzed the data with help of Y.M., J.Y., and R.M. T.M. performed the TTM analysis. All the authors discussed the results. R.M. and N.K. prepared the manuscript with substantial feedbacks from all the coauthors.

## **Competing interests**

The authors declare no competing interests.

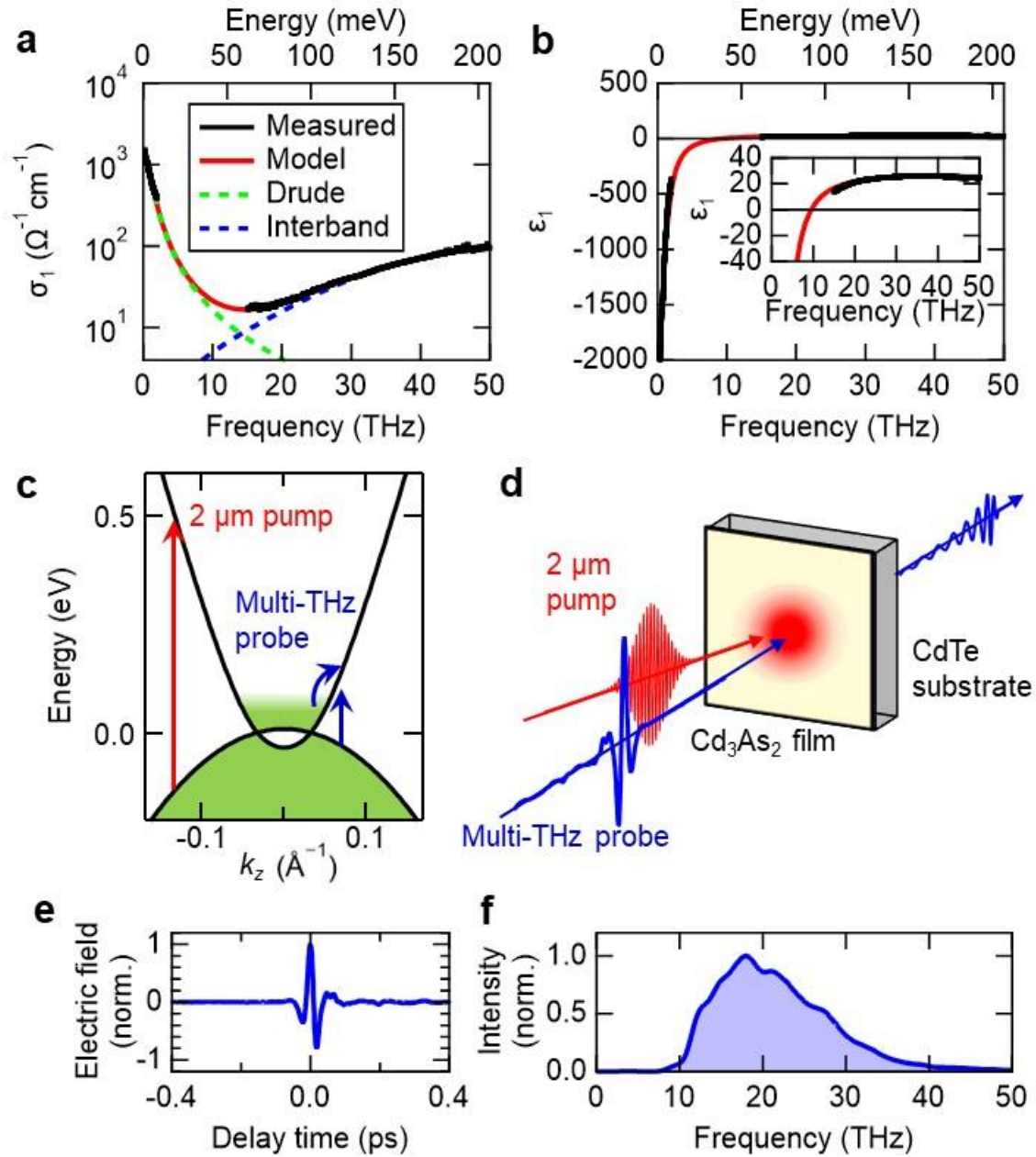


**Figure 1| Equilibrium response function in Cd<sub>3</sub>As<sub>2</sub> and experimental setup.** **a,b** Real-part optical conductivity and dielectric function in Cd<sub>3</sub>As<sub>2</sub> in equilibrium at room temperature. The thick black curves show the experimental data, and the red curves show fitted results. The green and blue curves show the weights of the Drude response and interband transitions, respectively. The inset in **b** is enlarged data to emphasize the zero-crossing point at the screened plasma frequency of 10 THz. **c** Model calculation of the band dispersion in Cd<sub>3</sub>As<sub>2</sub>. The red and blue arrows indicate NIR pump and multiterahertz probe, respectively. **d** A schematic of our experimental setup. **e,f** Waveform and power spectrum of the multiterahertz probe pulse.

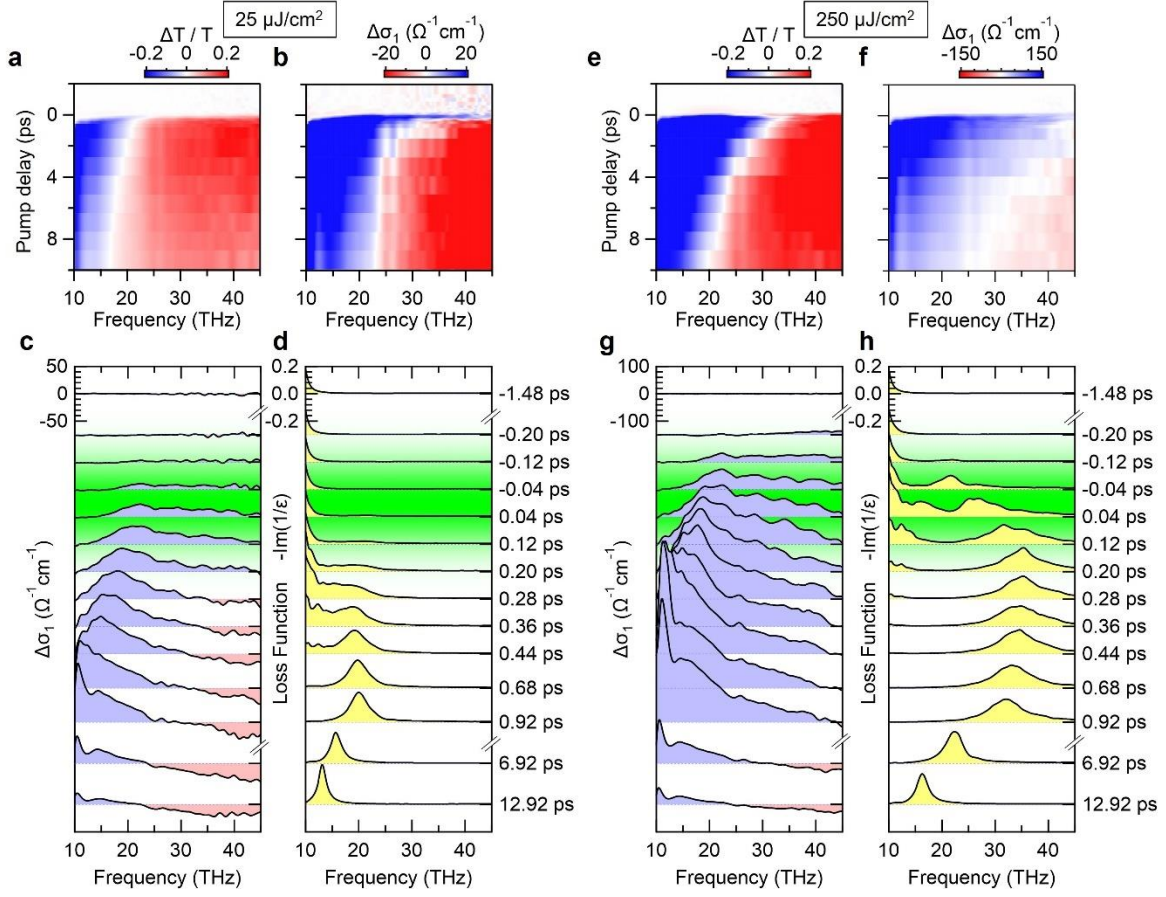


**Figure 2| Ultrafast change of conductivity and loss function spectra.** **a,b** 2D plots of differential transmittance  $\Delta T/T$  and differential conductivity spectrum  $\Delta\sigma_1$  as functions of frequency (horizontal) and pump delay (vertical) for the weak pump excitation regime of  $25 \mu\text{J}/\text{cm}^2$ . **c**  $\Delta\sigma_1$  at each pump delay. The green-colored region indicates the timing of the pump pulse irradiation. **d** Loss function spectrum  $-\text{Im}(\epsilon^{-1})$  at each pump delay. **e-h** The same sets of data for the strong excitation regime of  $250 \mu\text{J}/\text{cm}^2$ .

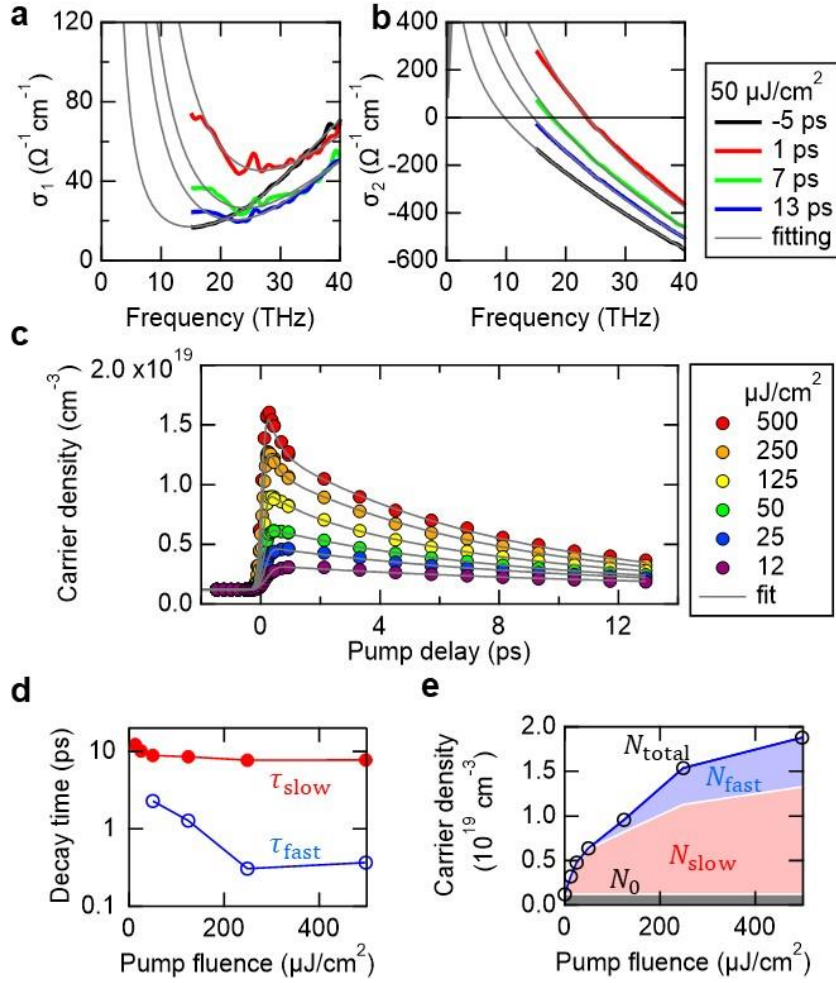


**Figure 3| Dynamics after thermalization (>1 ps).** **a,b** Real and imaginary parts of the conductivity spectra,  $\sigma_1$  and  $\sigma_2$ , for the excitation density of  $50 \mu\text{J}/\text{cm}^2$  at various pump delays. Thin black curves show fitted results using the Drude-type response and interband transition. **c** Dynamics of total excited carrier density as a function of the pump delay. The data are fitted by single and double exponential functions below and above  $50 \mu\text{J}/\text{cm}^2$ , respectively. **d** Semi-log plot of the decay times obtained in the fitting in **c** as a function of the pump fluence. **e** Total carrier density at the maximum  $N_{\text{total}}$  as a function of the pump fluence. The blue- red- and gray-colored areas ( $N_{\text{fast}}, N_{\text{slow}}, N_0$ ) correspond to the weights of fast and slow decaying components and originally doped electrons, respectively.

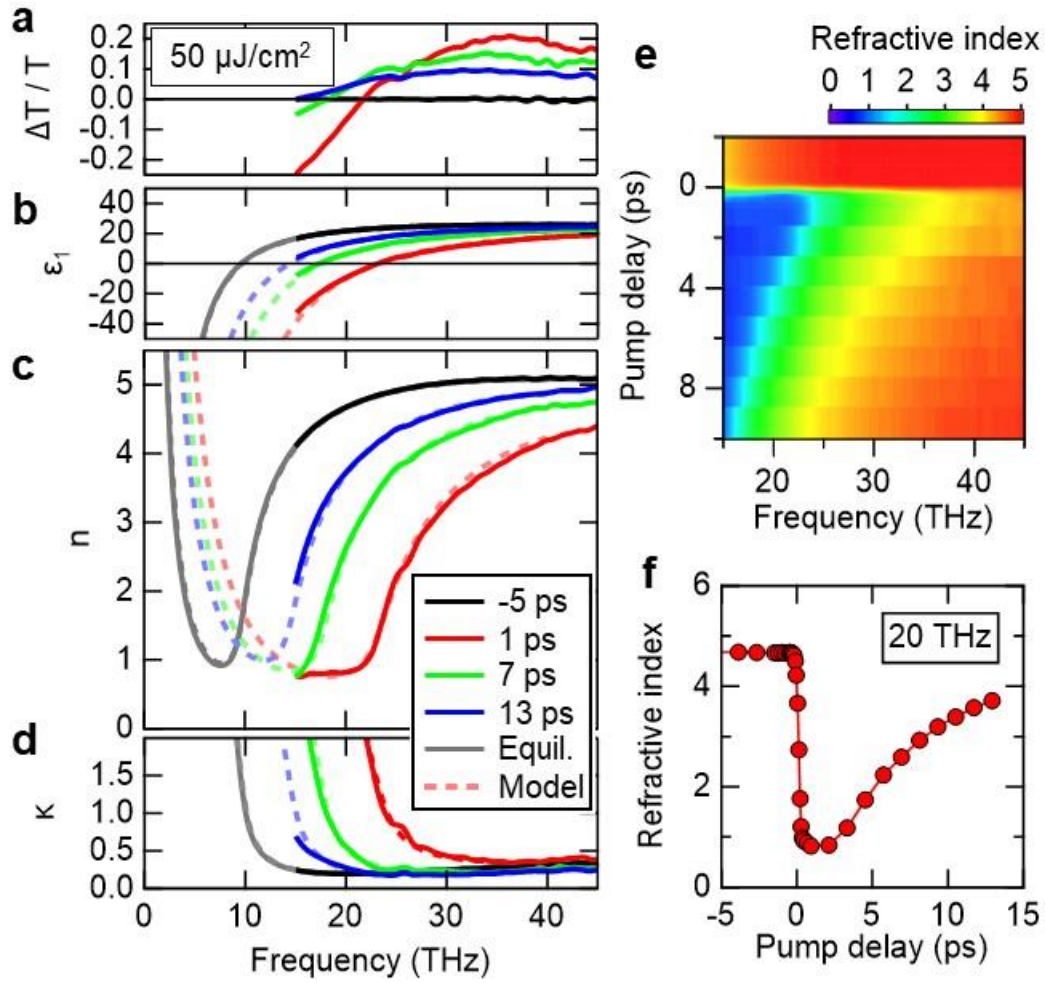


**Figure 4| Change of response functions.** **a-d** Transient transmittance  $\Delta T/T(\omega)$ , real-part dielectric function  $\epsilon_1(\omega)$ , refractive index  $n(\omega)$ , and extinction coefficient  $\kappa(\omega)$ , respectively, for various delays with the pump fluence of  $50 \mu\text{J}/\text{cm}^2$ . The broken curves show fitted results assuming the Drude response and interband transition. **e** 2D plot of the refractive index as a function of frequency (horizontal) and the pump delay (vertical). **f** Temporal evolution of refractive index at 20 THz as a function of the pump delay.